Chapter 2

HOLOGRAPHIC SPECTRUM SPLITTING

To move beyond the efficiency limits of single-junction solar cells, junctions of different bandgaps must be used to avoid losses from lack of absorption of low energy photons and energy lost as excited carriers thermalize to the semiconductor band edge. Over 40% of solar power incident on a single-junction solar cell is lost to one of these. [3] Spectrum-splitting photovoltaics mitigate these losses by incorporating multiple absorbers of different bandgaps. Tandem multijunction solar cell achieve high efficiencies but have challenges including current-matching and lattice-matching constraints and tunnel junction design required for each additional bandgap added. [4] Additionally high concentration makes thermal management challenging. Reference [6] has shown these factors can confer annual energy production advantages on collections of independently connected subcells. Such an arrangement is easier to achieve through lateral spectrum-splitting in which external optical elements are used to separate spectral bands. In addition to independent electrical connection, the thermal load of each cell is decreased by virtue of physical separation.

A common spectrum-splitting optical element is the Bragg stack. They are quite ideal spectrum-splitting optics as they can be designed to have sharp cutoffs in reflection and transmission to separate bands quite effectively without spectral band overlap, as can be achieved in tandem multijunctions in which subsequent cells are filtered by the absorption edges of higher bandgap cells. [8],[21] However depositing many dielectric layers of precise thickness is time-consuming and requires costly capital equipment. Holographic diffraction gratings, on the other hand, can be fabricated in a large area at high fidelity, motivating studies into holographic spectrum-splitting. High-efficiency designs demonstrating two-way splitting have been shown. [17]

Volume phase holograms have thicknesses much larger than their fringe spacings [22]. They can have diffraction efficiencies (intensity of total incident light to intensity of light going into the correct diffracted order) of up to 100% with low-absorption, low-scatter materials. In such gratings, the periodic index of refraction variation in the volume of the grating layer leads to phase differences in incident light resulting in diffraction. Among diffractive optics available, holograms have the advantage of avoiding complex lithographic fabrication steps. Hologram fabrication (using the exposure of a recording material to an interference pattern between coherent light sources) allows large-area fidelity of recording, creating a low-scatter, high-performance diffractive optic.

2.1 Methods

We use Moharam and Gaylord's 1977 generalized coupled wave analysis (GCWA) to model the holographic gratings [23]. GCWA neglects second derivatives of the electric field associated with each diffracted order (a slowly varying field approximation). Additionally, reflected diffracted orders are neglected. This leaves a system of 1st order, coupled linear differential equations to solve. This method gives the diffracted intensity in those output diffracted orders that are retained in the calculation. In our calculations, transmitted diffracted orders -7 to +7 have been retained. This large number has been retained due to diffraction into progressively higher orders as the initially normally incident solar light passes through each grating stack.

The GCWA approach balances accuracy and computational expense better than more conventional choices. Coupled-wave analysis, considering only the input (0th order) and 1st order output is a valid approximation when the angle of incidence is near the Bragg angle and the grating is thick. In our case of stacked gratings and very broadband illumination, there will be much incident light that is far from the Bragg condition, and so we need a broader theoretical formulation to consider diffraction from our gratings. Rigorous coupled wave analysis, on the other hand, gives a more accurate solution (it is exact for a grating of infinite area when an infinite number of diffracted orders are used) but is computationally expensive.

To model the full compound holographic spectrum splitter, the output of each successive grating in a particular stack is found using GCWA for normally incident light. The intensity of normally incident light diffracted into orders -7 to +7 by the top hologram is calculated and those orders with greater than 0.01% diffraction efficiency are retained and become an input into the second grating in the stack. Similarly the output of the second grating becomes the input into the third grating. Finally, the output intensities and diffraction angles from the final grating are used to determine which underlying solar cell any particular output from the bottommost grating will hit. The total output fraction of input light intensity hitting each cell can be converted to a photon flux using the AM1.5d spectrum to determine how many above bandgap photons are hitting each of the four tandem cells.

Holographic recording media

The holographic material is a key component of this design. We require low absorption and scattering over a broad wavelength range (300 nm - 1700 nm), high resolution, tunable properties, high diffraction efficiencies, and ease of processing. In addition to all this, incorporation into a solar application requires a long lifetime (>25 years), the ability to withstand high-intensity light without performance degradation, and resistance to the elements and to breakage. These criteria make dichromated gelatin (DCG) the top choice with its low absorption [24] and scattering and a wide range of index of refraction modulation (Δn). Common applications of DCG holograms include laser applications such as pulse compression, beam-splitting, and beam-combining, which require high light intensity exposure. DCG is hygroscopic and thus requires encapsulation. Additionally, the index of refraction modulation can vary from 0.01 to up to 0.4, but as this index modulation increases scattering into spurious diffraction orders also increases [22], so we have restricted the range of search from 0.01 to 0.06. Layers can be easily deposited and exposed at thicknesses less than 30 μm. All simulations used dichromated gelatin as the recording medium. Calculations assumed the refractive index of dichromated gelatin to be a constant value of 1.3 and the refractive index modulation to be sinusoidal. Edge effects in the holograms are assumed to be negligible.

DCG gratings are recorded on a substrate, in our case fused silica. During post-processing a superstrate is placed on top, and the edges are sealed with a moisture barrier for full encapsulation. The effective index of refraction of the DCG gratings is around 1.3 while the substrate, commonly fused silica or glass ranges from 1.45 to 1.55. The index of DCG during recording (before development), however, is 1.55. It is desirable to have an index-matched substrate during the hologram fabrication to avoid artifacts due to Fresnel reflections off the substrate during the recording process. Alternatively, having an index match during use in the grating stack reduces Fresnel reflections during the lifetime of the grating stack. This trade-off also incentivizes the use of holographic materials which can be better index-matched to available substrates and which do not require post-processing, which might alter their pre- and post-recording properties. There are holographic photopolymers, but none with the record of use or full set of desirable qualities of DCG.

Target spectral band selection and band gap energy dependent external radiative efficiency

Cell bandgap selection was done using a detailed balance model incorporating non-unity external radiative efficiency and non-unity current collection as variable parameters to approximate realistic cell performance according to [6]. We assume that only certain percentage of incident photons are absorbed and that the active materials have either a fixed external radiative efficiency (ERE) of 1% or 3% or a bandgap dependent ERE as described below. These de-rating factors account for losses such as non-radiative recombination and parasitic absorption and produce realistic cell efficiency estimates from the theoretical detailed balance calculation. The eight subcells of the four dual-junction solar cells shown in Fig. 2.5 have a combined de-rated detailed balance efficiency of 46.97% using these de-rated parameters of 90% absorption, 1% ERE for unconcentrated illumination and perfect spectral splitting. With a concentration of 100X this goes to 52.7%. The figure of merit for the splitting performance is the optical efficiency, defined as,

$$\eta_{optical} = \frac{System\ power\ with\ actual\ splitting}{Power\ with\ perfect\ splitting}, \tag{2.1}$$

where system power refers to the power obtained by independently connecting the four dual-junction cells and using DC-to-DC converters to combine the output current and voltage into a two-terminal output.

In order to appropriately select among available III-V semiconductor alloys, we extracted external radiative efficiency using experimental cell voltages. We used experimental data from our Full Spectrum Photovoltaics collaboration with Spectrolab lab as well as published data from Spectrolab [4] to extract external radiative efficiency using the reciprocity relation [25],

$$V_{OC} = V_{OC}^{rad} + kT \log(ERE), \tag{2.2}$$

where V_{OC} is the experimental open-circuit voltage, V_{OC}^{rad} is the open-circuit voltage expected in the radiative limit (internal radiative efficiency=1) according to the Shockley-Queisser detailed balance limit [1], k is the Boltzmann constant, and T is the cell temperature.

The simulated hologram output was propagated from the hologram output plane to the cell plane, and the output efficiency was weighted by the AM1.5D [26] spectrum to generate photon fluxes incident on each dual-junction cell. The iterative optoelectronic design process includes updating the ideal bandgaps of the four dual-junction cells to account for photon misallocation after design of the optical element.

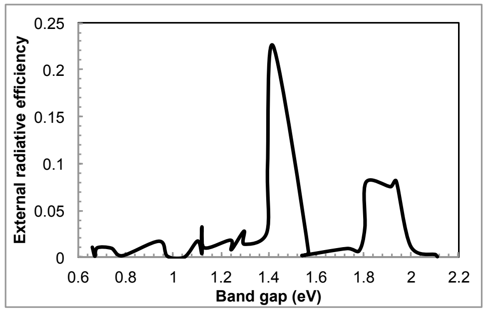

Figure 2.1: Band gap depdendent external radiative efficiency.

In order to re-optimize the subcell bandgaps based on the simulated input fluxes, the top cell bandgap was varied across all accessible values (0.7 eV to 2.1 eV) and used to find a corresponding current-matched bottom bandgap. We allowed thinning of the top cell if a current match could not be found without it. A lattice matching constraint that restricted both top and bottom bandgaps to either be above 1.41 eV or both below 1.34 eV was also implemented. The tandem pair generating the highest power of all was selected. Details of the target spectral bands are specified in 2.1.

Holograms were fabricated by Wasatch Photonics as a best effort to match our specifications. Angle-dependent transmission of the holograms was measured using the Scatterometry feature of a J. A Woollam VVase Spectroscopic Ellipsometer. The total collected light in these measurements were treated to remove Fresnel reflections from the front and back air/fused silica interfaces without anti-reflection coatings using 2.4.

Concentrating elements were simulated in commercial ray tracing program LightTools. Optimization was done by fixing the concentrator shape to an ideal compound parabolic concentrator (CPC) [20] with free parameters being the input angle, the trim, and input size. The output size was fixed at 1 mm as a minimum cell width. The CPC-height-to-cell-width ratio is set by the hologram diffraction angle and the CPC medium.

2.2 Results

Diffraction of a particular wavelength at a particular angle occurs at a given grating thickness, ϕ angle, refractive index modulation and grating line periodicity. If the grating thickness is modified from this optimum, the diffraction efficiency falls off. Similarly, as the diffraction efficiency falls off as the illumination wavelength changes from the design wavelength. All but the 0th order are dispersive, so the diffraction angle also changes with wavelength.

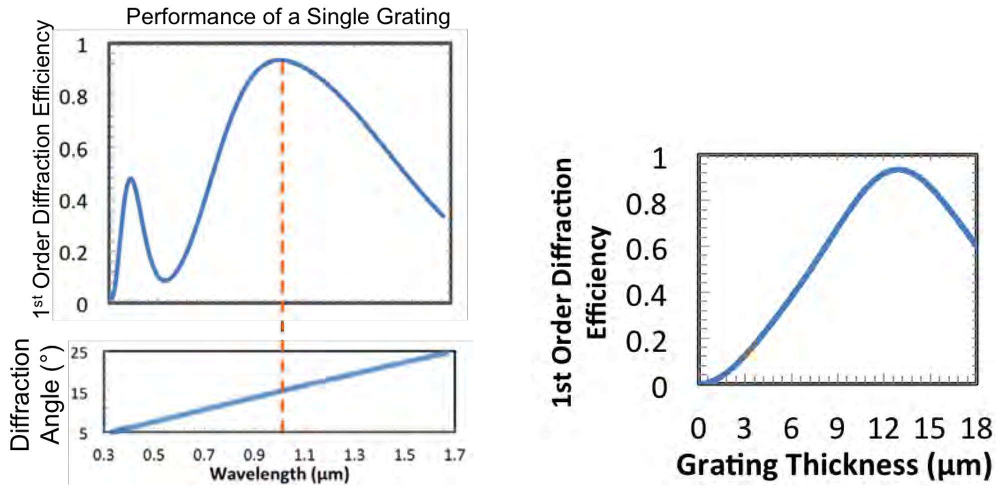

Figure 2.2: Diffraction efficiency and diffraction angle of a single grating as a function wavelength and grating thickness.

For a single grating, there is a minimum effective refractive index modulation for high diffraction efficiency for high first order diffraction efficiency. This is due to the thickness limit of dichromated gelatin holograms. As the diffraction angle increases, the effective path length within the grating increases and the maximum possible diffraction efficiency increases for the low modulation case. Also, because of this, the minimum needed refractive index modulation is higher for longer wavelengths.

Optimizing diffraction angle

For a given value of Δn there is a minimum effective thickness to get high diffraction efficiency. Thicker gratings and lower Δn give lower bandwidth diffraction peaks and likewise thinner gratings with higher Δn give higher bandwidth peaks. In order to select the primary diffraction angle which sets the aspect ratio of the holographic splitting module, the relationship between diffraction angle and diffraction efficiency was mapped. Fig. 2.3 shows first order diffraction efficiency as a function of first order diffraction angle, wavelength, and refractive index modulation Δn. Passing through a minimum effective grating thickness is needed for high diffraction efficiency. Effective thickness can be increased by increasing the diffraction angle or increasing Δn. For $\Delta n = 0.02$, the longer three wavelengths do not reach high diffraction efficiency, because the interaction between the incident beam and the grating is not enough to full couple the light into the first diffracted order. For higher values of Δn all wavelengths are able to couple into the first diffracted order with high efficiency when the first diffraction angle is between about 10° and 45°. Diffraction angles larger than 50° within dichromated gelatin will lead to diffracted light being totally internally reflected if there is an air-encapsulant interface between the holograms and the cells. While larger diffraction angles enable a smaller aspect ratio, they also increase the spread of angles hitting the solar cells increasing the burden on the cell anti-reflection coatings to perform for a larger angle range.

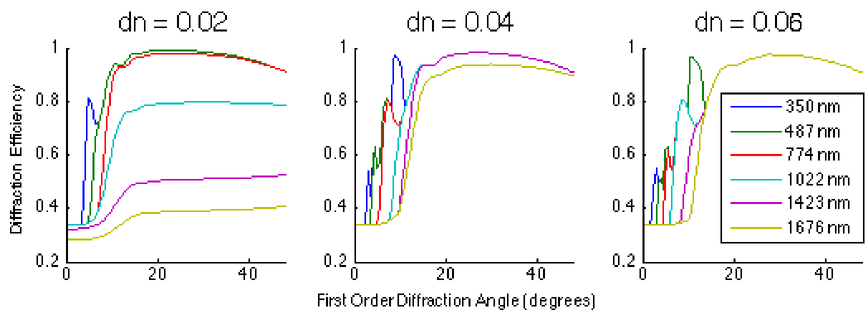

Figure 2.3: Peak first order diffraction efficiency for a given wavelength as a function of Δn, first order diffracted angle, and wavelength.

Two-way splitting design

We first consider the simpler problem of two-way holographic splitting using a single grating above each cell used to diffract the out-of-band light to the neighboring solar cell. As seen in Fig. 2.4, with only two single gratings placed one next to the other, intentional heuristic design is possible. In the top figure, two gratings are design to have their diffraction peaks aligned with the nulls of the other grating leading to diffraction peaks of light going to each cell at near unity. In contrast, if both gratings are diffracting in a certain wavelength range as is the case for short wavelengths here, poor separation occurs. In contrast, to this simple case, multivariate optimization is needed for the four-way splitter as the complexity is too high for a simple method. The greater number of subcells are needed, however, for the potential for high conversion efficiency.

2.3 Four-way holographic stack design

The Holographic Spectrum Splitter, shown schematically in Fig. 2.5, splits broadband, incident sunlight into four spectral bands, each targeted at a dual-junction solar cell with bandgaps tuned to best convert the incident spectral band. The transmissive holographic spectrum-splitting optical element is composed of 12 individual volume phase holographic diffraction gratings arranged into four stacks of three gratings. Each grating in a stack is designed to primarily diffract one band of light toward one of the three solar cells in the cell plane which are not directly underneath the hologram stack. The fourth spectral band is intended to pass through the three

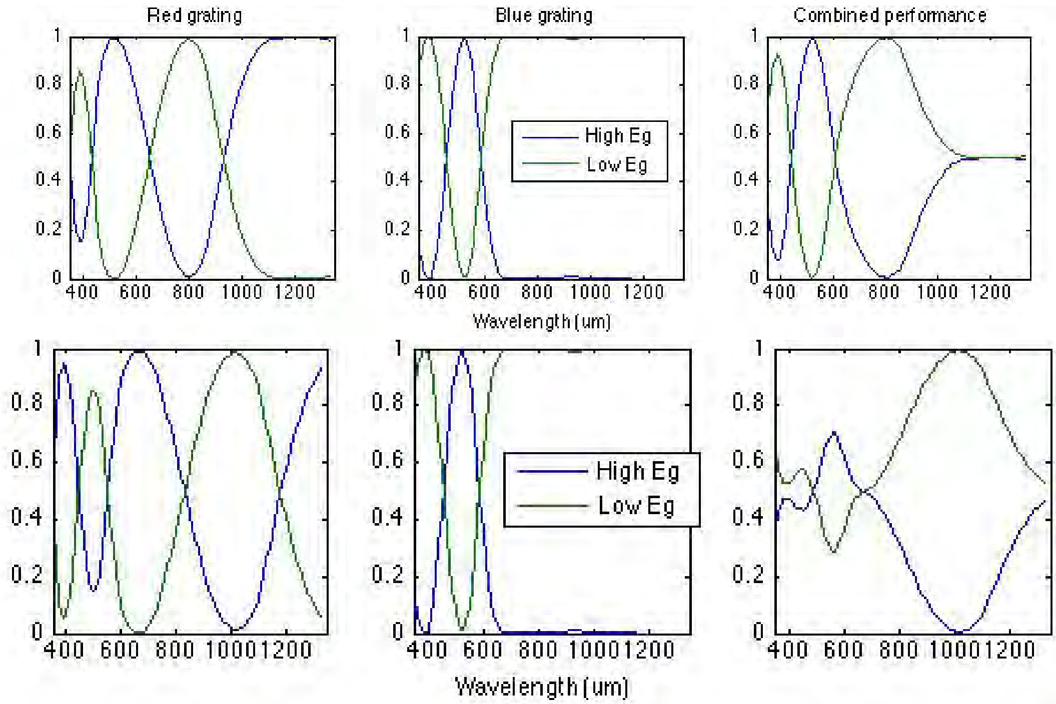

Figure 2.4: Plots show the fraction of light reaching either the high bandgap or low bandgap subcell in a two-way holographic splitter. The two left plots show results for two different designs for the 'Red grating' which sits above the higher bandgap subcell and diffracts longer wavelength light toward the lower bandgap subcell. The blue grating (center) is the same in both cases. When the fluxes hitting both cells are combined, the top grating pair is clearly complementary, while the bottom Red grating is a poor partner for the blue grating.

stacked gratings to the cell directly underlying the stack. Each grating stack sends the highest energy light incident on the stack toward the tandem cell designed for high-energy photons, and the lowest energy light incident upon it toward the right-most cell, designed for low-energy photons. The spectral bands and bandgaps of the top and bottom subcell in each tandem are given in Table 2.1. Lattice-matched III-V alloys can be found for each of these subcell pairs.

Band	Design λ (nm)	Bandwidth (nm)	Top bandgap (eV)	Bottom bandgap (eV)
1	487	300-674	2.1	1.84
2	774	675-873	1.6	1.42
3	1022	874-1170	1.23	1.06
4	1425	1171-1676	0.93	0.74

Table 2.1: Wavelength range of spectral bands

Each grating is designed for a particular wavelength within its spectral band. Holographic diffraction gratings have a decrease in diffraction efficiency as the wavelength deviates from this design wavelength as shown in 2.2. We aim to have the full width, half maximum of each diffraction peak equal to the desired bandwidth to get optimal diffraction of each band and minimize cross-talk between spectral bands.

Only the light at the design wavelength of a given grating will get diffracted to the correct angle. As the wavelength deviates slightly from the design wavelength, so too does the angle corresponding to the output diffraction order shift slightly. As the wavelength increases the diffraction angle increases. Thus in the spectral band in which 874 nm to 1170 nm light is to be diffracted 10 deg, the 970 nm light will go 10 degrees, the 874 nm light will go < 10 deg and the 1170 nm light will go > 10 deg. Thus most of the light is falling not just on the intended cell, but also onto one of its neighbors. Photons falling on cells with bandgaps to the blue of their energy will not be absorbed at all while photons falling on cells with bandgap to the red of their energy can get collected and generate some energy. Additionally the more energetic spectral band contains the most power, so it is most important that this band get to the correct cell. The extended structure of the array is a head-to-head, tail-to-tail arrangement, to minimize photons going to cells of completely different bandgaps. This dependence of output angle on wavelength and this extended geometry are accounted for in our holographic simulations.

The individual gratings have four design parameters shown in Fig. 2.5a: grating fringe tilt angle Φ, periodicity L, amplitude of index of refraction variation Δn, and grating thickness d. The individual gratings are encapsulated and combined into a stack using optical adhesive as shown in Fig. 2.5b. The idealized splitting of Stack 2, the second grating stack from the left is shown in Fig. 2.5c along with size ranges for various components and the optimized bandgaps for an ideal split of the AM1.5D spectrum [26]. The eight subcells are composed of group III-V semiconductor alloys, latticed matched to either GaAs or InP as growth substrates. Angle θ_1 is selected to be 10° based on simulations of single gratings subject to a maximum thickness of the holographic recording medium of 18 μm, the results of which are shown in Fig. 2.3. The diffraction angles θ_2 and θ_3 are calculated assuming four equally-sized tandem solar cells and constant distance between the cell plane and output plane of the holograms.

For highest efficiency, both high optical efficiency of spectrum splitting and concentration are required as seen in Fig. 2.7a. Fig. 2.7c shows the strong angle

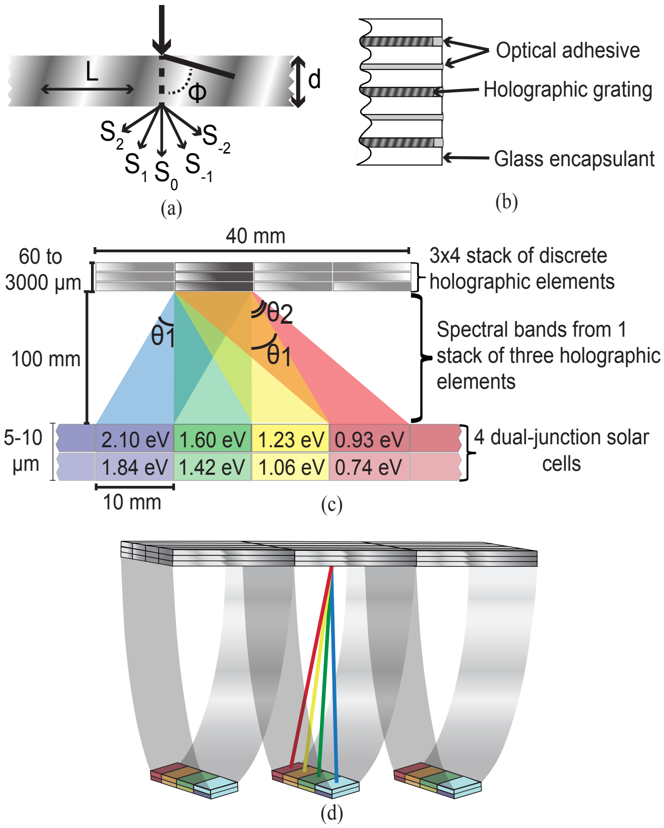

Figure 2.5: (a) Schematic of volume phase hologram of thickness d with write and gray fringes representing varying refractive index with periodicity L, tilted with respect to the grating normal by angle Φ. Normally incident light S_{inc} is split into a series of diffracted orders S_i.(b) Encapsulated holograms are glued into a stack of three with optical adhesive (c) Four stacks of three holographic gratings are assembled into a spectrum-splitting optical element. Each stack generates four spectral bands, one from each grating and a fourth that passes straight through the three-grating stack. Spectral bands are coupled into one of four high-efficiency III-V alloy, dual-junction solar cells tuned to best convert the target band of light. (d) Trough compound parabolic concentrators concentrate light after splitting in the direction orthogonal to frequency splitting. Individual spectrum splitting submodules tile to form a photovoltaic module.

sensitivity of the spectrum-splitting element, leading us to correspondingly design concentrating optics for a 1° acceptance half-angle. Concentration is incorporated orthogonal to the plane of spectrum splitting using a trough compound parabolic concentrator (CPC). Individual submodules can be tiled one next to the other into a module as shown in Fig. 2.5d.

Φ and L are chosen to fulfill the grating equation for the central wavelength of each spectral band for normally incident light.

Grating thickness and Δn were optimized by multiple strategies presented below.

Vary minimum diffraction angle for fixed index modulation

Despite the earlier result that higher refractive index was necessary for single gratings to achieve high diffraction efficiency, when combined into a 12-grating array which interfere with one another, lower modulation for each grating yields better overall results to avoid stronger interference effects.

Fix dn for all Gratings, pick d for central λ

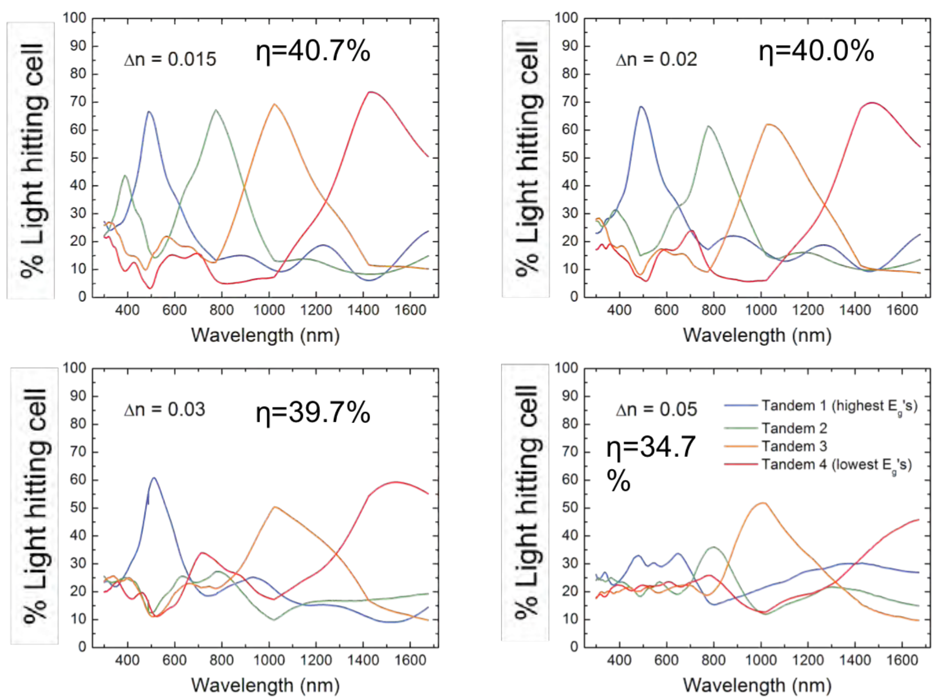

Figure 2.6: System performance for varying Δn.

The flux hitting each cell becomes the input to detailed balance calculations, which give a conversion efficiency for the sub-module. The grating model accounts for any misallocated photons due to the optics. The parameters of the holographic spectral splitter grating are given in 2.2. The index of refraction variation Δn=0.015 is used for all of the gratings. Recognizing that the optimal current matched tandem cells for the actual spectral bands generated from the splitting optics will not be the same as the best bandgaps for perfect splitting, the bandgap selection is re-optimized. This gives bandgaps of 2.24 eV/1.38 eV for the top cell, 1.74 eV/1.12 eV for the second highest, 1.36 eV/0.94 eV for the third tandem, and 1.06 eV/0.75 eV for the lowest energy tandem. These pairs are current-matched but not lattice-matched. Including realistic cell performance with 90% absorption and 1% external radiative efficiency de-rating factors at the cell level and the splitting of the holographic stacks, the total system efficiency with the re-optimized bandgaps and 380x concentration is found to be 43.19%. The optical efficiency of these holograms is found to be 78.80%. A 5% loss due to Fresnel reflections between the gratings and their substrates, off the front face of the cells, and from the interface between the two CPC stages is assumed. A 2% series resistance due to electrical contacts and an additional 2% due to power conditioning electronics are assumed[27]. Finally the losses due to the concentrators are estimated to be 8.3%. All together the sub-module is expected to have a realistic efficiency of 36.14%.

Vary dn, pick d for central wl

The grating thickness was selected to maximize the diffraction efficiency of the central wavelength going into the first diffraction order for a given Δn. A parameter sweep was done over Δn values and over the order of the three gratings in each stack to optimize the value of a figure of merit which power weights the percentage of photons hitting the correct subcell. We define it as

$$FOM_i = V_i \times flux_i(\lambda) \times \eta(\lambda), \tag{2.3}$$

where i is the spectral band, V_i is a lower bound for open-circuit voltage of subcell i estimated by the bottom bandgap of the subcell minus 400 meV, $flux_i(\lambda)$ is the portion of the AM1.5D spectrum in band i, and $\eta(\lambda)$ is the fraction of in-band incident light reaching the solar cell.

This figure of merit was evaluated over 58 wavelength points over the solar spectrum (300 nm-1700 nm) with 24 nm spacing. Δn was varied between 0.01 and 0.06 by 0.005 for stacks 1 and 2 and between 0.015 and 0.055 by 0.01 for stacks 3 and 4 yielding up to 11 possible values. Additionally, the three gratings could be stacked in six possible permutations giving ≤7986 configurations for each of the four grating stacks. Each parameter combination was evaluated, and the results were sorted by the figures of merit of the stacks. The output fluxes of the eight best parameter combinations for each stack were combined giving $8^4 = 4096$ combinations which were evaluated using a detailed balance re-optimization of the bandgaps for the actual flux hitting each cell (described in Section 2.1). The twenty best parameters sets for the holographic splitting element were then simulated with wavelength spacing of 1 nm. Through this process, an optimized set of grating specifications, given in Table 2.2, was determined. The resulting spectral separation is shown in Fig. 2.7b, where the fraction of incident light hitting each of the four subcells is shown along with dashed vertical lines showing the position of the absorption cutoffs for the top and bottom solar cells re-optimized for the actual flux they are receiving under the holographic splitting element. The bandgaps are also given in Fig. 2.7d.

Table 2.2: Optimized holographic splitting element grating parameters

	λ_c (nm)	Φ (°)	L (μm)	d (μm)	Δn
Stack 1	1423	-77.0	2.43	18.0	0.01
	1022	-80.6	2.40	17.1	0.03
	774	-85.0	3.42	18.0	0.015
Stack 2	487	85.0	2.15	16.1	0.015
	1022	-85.0	4.51	18.0	0.015
	1423	-80.6	3.34	18.0	0.03
Stack 3	487	80.6	1.14	4.4	0.055
	1423	-85.0	6.28	18.0	0.045
	774	85.0	3.42	18.0	0.015
Stack 4	487	77.0	0.83	4.5	0.055
	1022	85.0	4.51	18.0	0.015
	774	80.6	1.82	18.0	0.015

Experimental Results

The holographic recording medium, dichromated gelatin, is hygroscopic and must be encapsulated for the holographic diffraction grating to persist. The holographic gratings fabricated here are sandwiched between 1 mm fused silica slides with Norland Optical Adhesive as an edge barrier, as illustrated in 2.5b.

The three gratings of Stack 1 were fabricated, and the diffraction efficiency of each grating was measured as a function of diffraction angle and wavelength. Fig. 2.8 shows the diffraction efficiency of each order for the four fabricated gratings with $\lambda_c = 1022\ nm$. In addition to the diffracted orders, the summed transmission is shown at the top. At the peak of the first order diffraction efficiency, all transmitted light is going into the first diffracted order. In contrast the grating designed for $\lambda_c = 1423\ nm$ was optimized into invisibility. This is most evident in comparing the simulated flux going through Stack 1 to each of the four tandem subcells with and without the $\lambda_c = 1423\ nm$ shown in Figure 2.9. Given the realistic losses associated with passing through an additional grating layer, the final experimental results presented here exclude this grating and focus on a two-grating stack.

Total transmission and specular reflection measurements of the fabricated gratings were also taken. Fig. 2.10a and 2.10b show color plots of diffraction efficiency

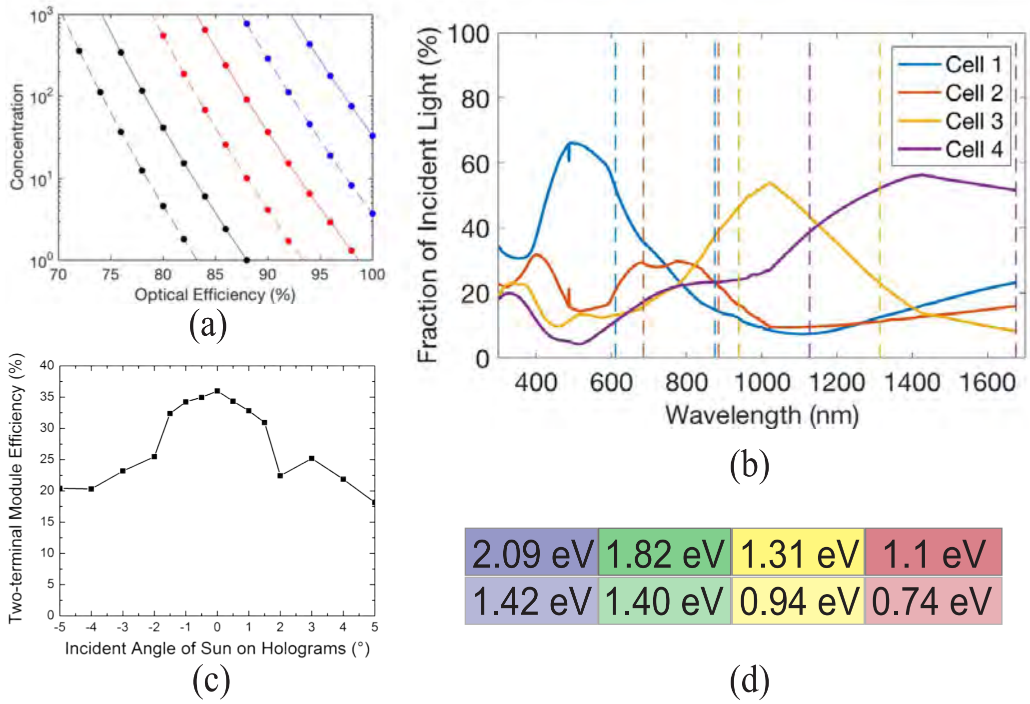

Figure 2.7: (a) Contours of 40% (black), 45% (red) and 50% (blue) module efficiency for aggressive cell performance targets (solid) of 3% ERE and 92.5% of ideal absorption and moderate cell performance targets (dashed) of 1% ERE and 90% of ideal absorption as a function of optical efficiency of spectrum splitting, concentration, and cell performance, (b) Percentage of incident light hitting each of the four tandem solar cells after passing through optimized holographic splitting element. Vertical lines correspond to the re-optimized bandgaps of the dual junction solar cells that optimize device performance for the actual incident flux hitting each solar cell, (c) Holographic splitter and concentrator performance as a function of incident angle. A tracking accuracy of 1° is sufficient to retain >93% system performance. (d) Re-optimized bandgaps of four dual-junction cells based on actual spectral bands from (b).

versus wavelength and diffraction angle for the experimental and simulated grating stacks, respectively. In order to isolate the spectral match-up of the simulated and experimental gratings, scattering and absorption losses were extracted from total transmission measurements and added to the simulated results as described in the Methods Section. Additionally, polarization averaged normal incidence Fresnel reflections from the front face R_f and diffraction-angle dependent Fresnel losses from the back interface R_b were removed from the measured transmission results T_m to get the Fresnel corrected transmission T_c from

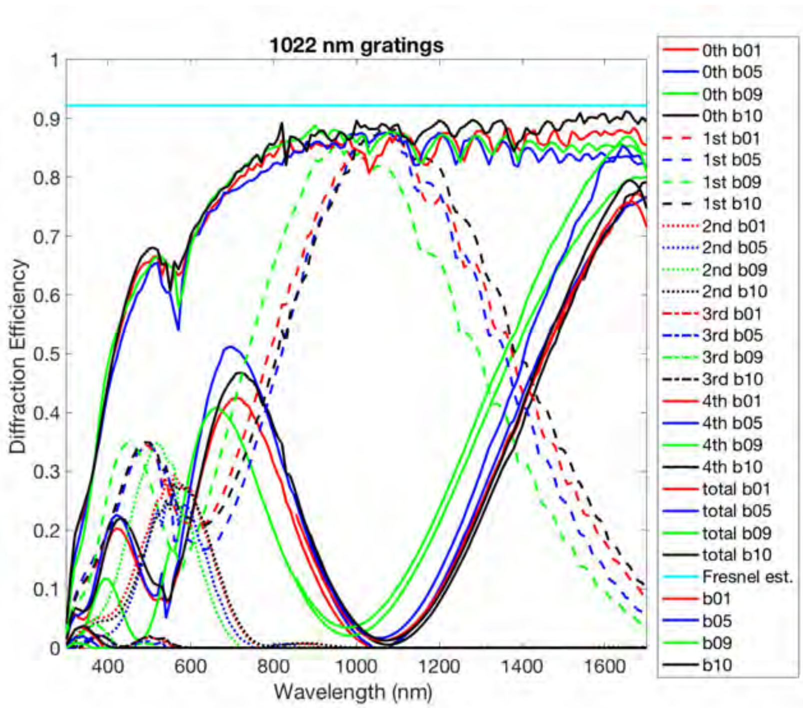

Figure 2.8: Measurement results for four $\lambda_c = 1022\ nm$ gratings. Each color represents a different grating and each line style shows a different diffracted order. The cyan line at 0.92 represents a rough approximation of expected Fresnel reflection loss.

$$T_c = \frac{T_m(\lambda, \theta)}{(1 - R_f(\lambda)) \times (1 - R_b(\lambda, \theta))}. \tag{2.4}$$

This dataset, like for the simulation results above, was converted from intensity as a function of wavelength and angle leaving the hologram plane to flux hitting the subcells by propagating the diffraction efficiencies to the cell plane and weighting by the AM1.5D reference spectrum. The fraction of photons hitting subcells 1 to 4, where 1 is the highest bandgap tandem and 4 the lowest bandgap tandem, determined by simulation and experiment with correction are presented in Fig. 2.10c-f, respectively, along with total transmitted light in both cases shown in Fig. 2.10e.

Concentrator Design

The holograms are sensitive to the angle of incidence of light, and this sensitivity is increased when stacking holograms, which act in concert. Thus, they must be incorporated into a tracker. The submodule performance drops off significantly for

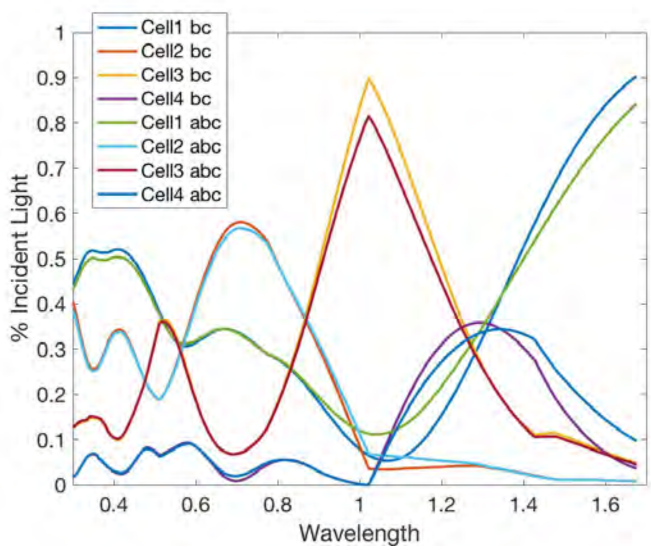

Figure 2.9: Fraction of light going into each subcell versus wavelength. The discrepencies between the two stacked gratings (bc) and the three stacked gratings (abc) are minimal.

light incident at a deviation of greater than 2° from normal. This angular sensitivity is similar to that of high-concentration optics. Since using angle-of-incidence sensitive diffractive optics requires tracking of the sun and use of only the light in the direct solar spectrum rather than the global solar spectrum, concentration allows both a compensation for the diffuse light lost as well as the potential to access much higher overall efficiencies.

Increasing concentration, holding all else constant, improves efficiency. Additionally, concentration allows smaller active device areas and thus lowers cell costs. Non-imaging optical elements allow concentration that can reach thermodynamic limits [20]. A compound parabolic concentrator (CPC) takes any light incident on its input aperture within a certain half-angle (its acceptance angle) from the normal and reflects it to its output aperture. In the concentration scheme used for the holographic splitter (2.5), the top CPC is a curved, silvered mirror, which concentrates light orthogonal to the direction of spectral splitting. The secondary CPC is concentrating in two directions with rectangular input and output apertures. It is solid and made of a high-index polymer (n=1.65) giving an n^2 enhancement in the concentration relative to a hollow CPC with the same acceptance angle. The reflection at the surface of the CPC is due to total-internal reflection at the polymer-air interface. The rectangular shape comes from intersecting two trough CPC profiles. The inset shows the shape of the secondary concentrator. The corners add some loss

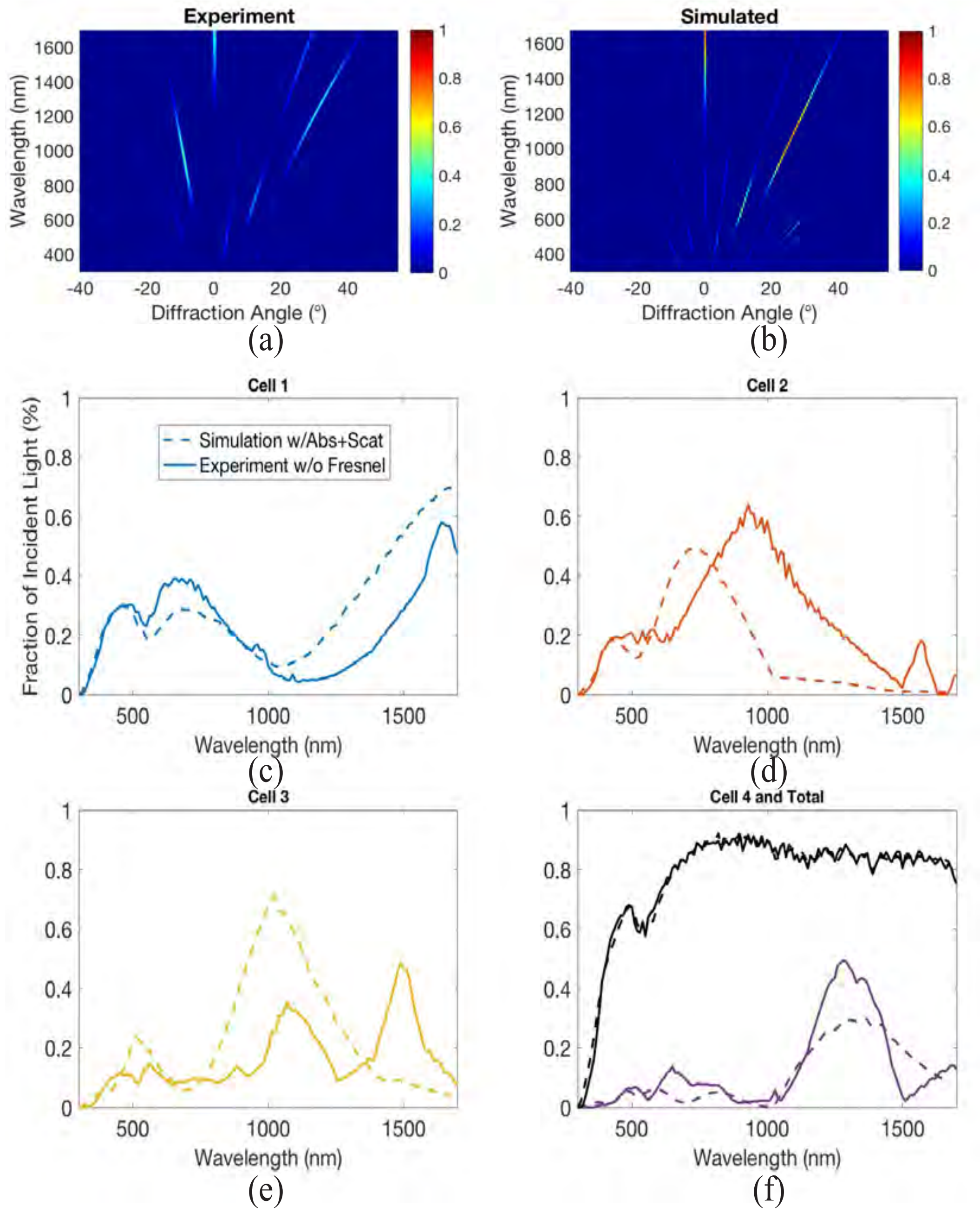

Figure 2.10: Color plots showing spectral and angular spread of (a) measured and (b) simulated light going through one grating stack (Stack 1). (c-f) Fraction of light hitting each solar cell after passing through the grating stack in simulation (dashed) and experiment (solid) with Cell 1 as the highest bandgap tandem and cell 4 being the lowest bandgap tandem. (f) additionally shows the total light transmitted through the stack.

relative to a trough that concentrates in only one direction. The optimum output to the cells accounting for both increased concentration and increased loss from the concentrator must be balanced.

We use trimmed trough compound parabolic concentrators (CPC) as concentrating elements in the direction orthogonal to the spectrum-splitting direction [20]. The angular spread of light exiting the concentrator is limited to 50° using a conical section at the CPC output to minimize Fresnel losses at the cell/concentrator interface. The spectrum splitting itself incorporates an additional factor of 4X concentration. A hollow, silver-coated trough, solid quartz, and solid PMMA trough CPC were optimized. Total concentration and transmission efficiency of the external concentrator are given in 2.3.

The concentrator transmission efficiency and the simulated photon flux hitting each subcell are used to simulate module efficiency. We account for losses including misallocation of light due to the holographic spectrum splitting, Fresnel reflection loss, non-unity external radiative efficiency of the solar cells (detailed in Section 2.1), imperfection collection of incident light on the cells (92.5%), 98% power conditioning efficiency [27], and 2% series resistance loss. For the front air-fused silica interface, the normal incidence reflectivity of an optimized anti-reflection coating is assumed to be 99% across the solar spectrum. At the back air-fused silica interface with an additional need for anti-reflection for a broad angle range, a reflectivity of 98.5% is assumed. Finally at the cell input face an angle and spectral averaged transmission of 97.5% is assumed for a total of 5% Fresnel reflection losses. The optical adhesive used to glue the three gratings into a stack is assumed to be perfectly index matched and lossless.

The range for projected experimental module efficiency comes from averaging the total transmission of all the fully characterized experimentally made holograms, correcting for Fresnel reflections, and using the corrected average total transmission as a proxy for all unaccounted for losses. This maximum transmission cubed was applied to the simulated fluxes to give the bottom end of the range and this factor squared and applied to ideal spectral bands gives the top end of the range.

2.4 Discussion

Individual grating diffraction profiles of volume phase holograms can have quite high peak diffraction efficiency at the intended angle and design wavelength. This is evident in Fig. 2.8 at its peak all light transmitted through the $\lambda_c = 1022$ nm grating is going into the first diffracted order. As the incident angle or wavelength varies, however, the diffraction efficiency decreases smoothly in either direction.

Table 2.3: Simulated and projected module efficiency

Configuration	Concentration	Concentrator efficiency	Simulated module efficiency	Experimental efficiency projected
No external concentration	4X	100%	35.2%	
hollow trough CPC	101.3X	96.0%	36.8%	27.2%-39.5%
solid quartz trough CPC	121.2X	97.4%	37.54%	27.8%-40.2%
solid PMMA trough CPC	19.0X	95.4%	34.93%	

Additionally, diffracted orders (as opposed to the directly transmitted beam) are dispersive. As such, the angle at which light is diffracted varies as the wavelength varies. Both of these factors lead to the sloped fraction of light profiles in 2.7a and 2.7b, and thus the overlap of top and bottom bandgaps of adjacent tandem subcells bandgaps after re-optimization for actual splitting. This smeared out partial separation limits the amount of thermalization loss that can be compensated by converting higher energy photons in higher band gap cells and vice versa. A more ideal spectrum splitting element would have a more square reflection profile with sharper cutoffs. Reference [28] has shown that incorporating some concentration immediately below the hologram plane of a single holographic elements allows this problem to be partially overcome.

The current design for four-way splitting based on three stacked gratings and four dual-junction solar cells was motivated by pursuit of >50% module efficiency. Given the currently achieved design with losses originating mainly from optical losses it is possible that a redesign cutting the number of gratings or spectral bands would result in sufficiently higher optical efficiency to give a net efficiency benefit to a less ambitious design. As an example a two-way splitting design is presented in the supplementary information.

The experimentally fabricated hologram stack represents a first prototype rather than the best possible outcome. After absorption, scattering and Fresnel reflection losses are reconciled between simulated data and experimental data as described above, the most notable difference between the simulated stack results and the experimental results is a negative order peaked around 900 nm which pushes much light intended for cell 3 into cell 2. Measurements indicate this spurious order to be due to diffraction of light by the third grating which enters grating 3 in the first diffracted order of grating 2. While simulations accounted for such cross-talk, this diffraction, present in the experiment and not the simulation, indicates a deviation between the experimental and simulated results. Iterating the fabrication process should better reconcile the experimental results to the intended designs. For this reason, in making the projection for experimental module efficiency, we apply the Fresnel-corrected average transmission of the experimental gratings. This way, we incorporate losses such as grating scattering and absorption but not spectral mismatch between the simulated and fabricated gratings. The lower end of the projected range is the three-grating correction applied to the simulated fluxes while the high end of the range is the two-grating correction applied to ideal splitting.

The degree of concentration incorporated for the different concentrator types is constrained by many factors. For the solid quartz trough, weight is the primary concern. We limit the height of the concentrator to about 27 cm, giving an eventual module height of about 30 cm. For the solid PMMA trough, the height is significantly limited by absorption in the polymer. The height in this case is limited to 0.7 cm giving a power weighted solar absorption of 3.3% in the concentrator material. On the other hand, the hollow silver-coated trough CPC incurs metal absorption losses rather than volumetric losses, so the height is much larger 17.3 cm. However, the higher transmission efficiencies are for a higher degree of trim as less light hits the silver surface at very shallow, grazing incidence, minimizing absorption to 2.7%.

The optical efficiency of the concentrator is the key determiner of improved system efficiency. While 100% efficiency 90X concentrator and a 90% efficiency 100X concentrator give an equal current density at the cell plane, the former is much preferred from an overall energy conversion standpoint. Concentrator transmission losses directly cut down on cell current and thus also cell voltage. Thus increasing the degree of concentration at the expense of the transmission efficiency of the concentrator does not pay off for system efficiency.

Conclusion

Transmissive, volume phase holograms were explored as a spectrum splitting optical element. Optical recording confers benefits of avoiding mechanical fabrication

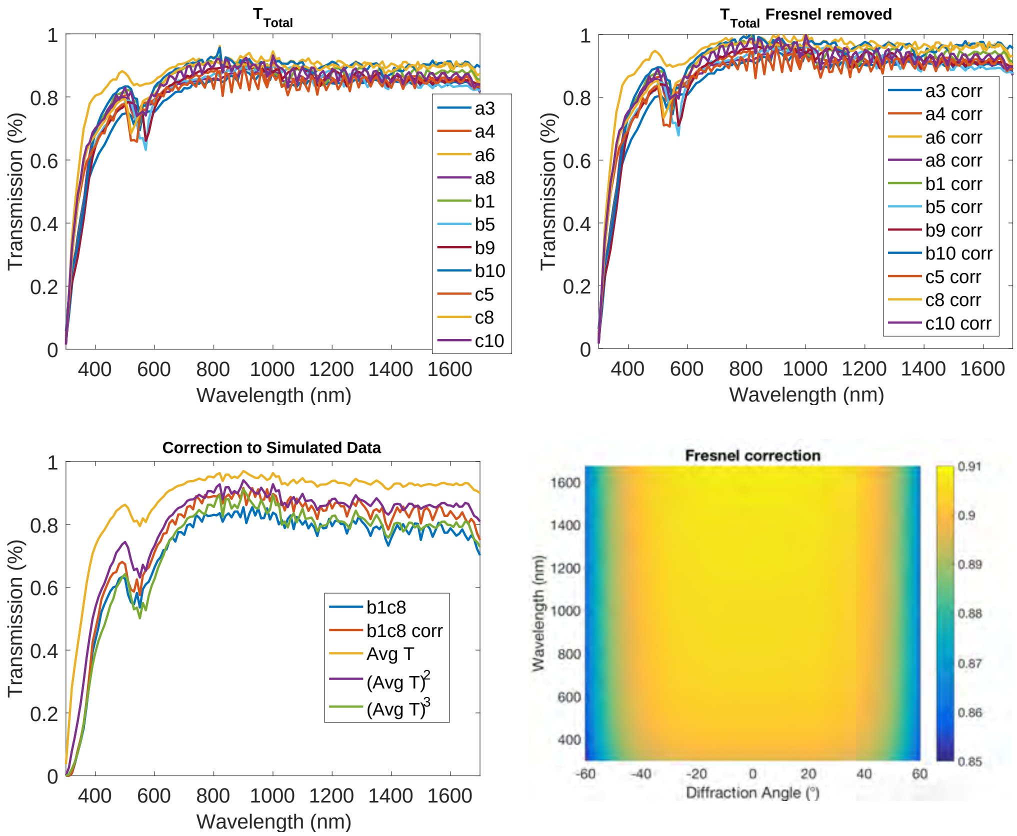

Figure 2.11: (top left) Total transmission as a function of wavelength for 11 fully characterized experimentally fabricated gratings. (top right) Total transmission treated with Fresnel correction (two normal-incidence air-glass interfaces). (bottom left) Average transmission through the eleven experimentally fabricated gratings after Fresnel correction applied plotted with this same transmission squared and cubed to approximate transmission through two and three-grating stacks. Also shown are the transmission and Fresnel corrected transmission for the two-grating stack. (bottom right) Fresnel reflection correction applied as a function of wavelength and diffraction angle.

defects. Additionally, these gratings can funnel all diffracted light into a single diffracted order for a single wavelength and diffraction angle. A holographic spectrum splitter design is presented which uses four stacks of three gratings each. Separated light hits one of four dual-junction solar cells for a total of 8 bandgaps. Grating simulations use generalized coupled wave analysis to track normally incident broadband light as it passes through and is diffracted by each grating in the stack. Simulated module efficiencies for this design can hit 37% including reflection, electrical, non-unity radiative recombination, and non-unity current collection losses.

Experimental demonstration of one of four three-grating stacks shows a fair match with simulated targets. It sets a lower bound for experimental realization of the design, since no iteration was done on the gratings. The experimental data are used to extract a spectrally dependent grating transmission function which is used to project a lower bound efficiency for a fully realized module.

Currently, the best simulated efficiency designs match current experimental records for lateral spectral splitting and for traditional tandem multijunction CPV modules. Thus future design efforts should focus on bringing up the efficiency even further. Incorporating lenses to decrease deleterious effects of dispersion in diffracted orders could improve efficiency significantly. Additionally, given the experimental measurement of grating losses, decreasing interface reflections and iterating on the hologram design toward a parameter set which transmits more light across the spectrum is necessary.